Imaging and Modulating Antisense Microdistribution in Solid Human Xenograft Tumor Models

Joseph D. Mocanu,[1,3] Kenneth W. Yip,[1,3] Julia Skliarenko,[1] Wei Shi,[1] Pierre Busson,[5] Kwok-Wai Lo,[6] Carlo Bastianutto,[1] and Fei-Fei Liu[1,2,3,4]

Abstract

Purpose: The tumor microenvironment is complex and heterogeneous, populated by tortuous irregular vasculature, hypoxic cells, and necrotic regions. These factors can all contribute to the biodistribution difficulties encountered by most cancer therapeutic agents. Antisense oligodeoxynucleotides (ASO) are a class of therapeutics where limited information is available about their distribution within a solid tumor environment.

Experimental Design: To assess ASO distribution, a fluorescein-labeled phosphorothionated ASO based on the G3139 mismatch control was injected systemically (i.v.) into tumor-bearing severe combined immunodeficient mice. Hoechst 33342 was injected i.v. to visualize active vasculature. Unstained sections were imaged through tiled fluorescence stereomicroscopy and then quantitated using novel algorithms. Tumor sections from four human tumor models were examined (CaSki, DU-145, C666-1, and C15) for hypoxia, apoptosis/necrosis, and morphology.

Results: For all four tumors, ASO accumulated within regions of hypoxia, necrosis, and apoptosis. Scatter plots of ASO versus active vasculature generated for each individual tumor revealed a consistent pattern of distribution of the ASO within each model. In C666-1 xenografts, the slopes of these scatter plots were significantly reduced from 0.41 to 0.16 when pretreated with the antivascular agent ZD6126 48 h before ASO injection. This was accompanied by the formation of large disseminated necrotic regions in the tumor, along with a 13.1 mmHg reduction in interstitial fluid pressure.

Conclusions: These data suggest the possibility that these algorithms might offer a generalizable and objective methodology to describe the distribution of molecular therapeutic agents within a tumor microenvironment and to quantitatively assess distribution changes in response to combination therapies.

Anticancer drugs are typically delivered systemically and must penetrate solid tumors at sufficient concentrations to reduce cell viability. The irregular vascular density and blood flow in tumors lead to varying rates of drug delivery. Tumor vasculature is tortuous, with long intercapillary distances; vascular shunts are common, allowing blood to pass directly from arterioles to venules (1–3). Blood flow through tumor capillaries is often slow, and at times, the direction of flow might even be stationary or reversed (3), leading to areas of necrosis (4). The observation of the distribution of necrotic regions relative to distant blood vessels led to the identification of tumor hypoxia (5, 6), which selects for cells resistant to apoptosis, and up-regulation of drug resistance genes (e.g., *P-glycoprotein*), thereby altering distribution of exogenous therapeutic agents (5, 7). Elevated tumor interstitial fluid pressure (IFP), a consequence of the irregular tumor vasculature, is another barrier to biodistribution; the escape of fluids from leaky vessels could disrupt the pressure gradient between blood vessels and the interstitium, thereby reducing mobility of solutes into and within tumor tissue (8, 9). Hence, the distribution of therapeutic compounds within the complex *in vivo* tumor microenvironment is significantly influenced by these important variables.

A class of therapeutic molecules in recent use is antisense oligodeoxynucleotides (ASO), which have shown promising results in clinical trials (e.g., G3139 and Bcl-2 antisense; refs. 10, 11). We have previously observed Bcl-2 antisense efficacy in preclinical human xenograft models of nasopharyngeal carcinoma (12), hence were interested in evaluating the distribution of these molecules in greater detail. To that end, we developed novel algorithms that quantitate the distribution of ASOs

Authors' Affiliations: [1]Division of Applied Molecular Oncology, Ontario Cancer Institute and [2]Department of Radiation Oncology, Princess Margaret Hospital, University Health Network; Departments of [3]Medical Biophysics and [4]Radiation Oncology, University of Toronto, Toronto, Ontario, Canada; [5]UMR 1698, Institut Gustave Roussy, Villejuif, France; and [6]Department of Anatomical and Cellular Pathology, Chinese University of Hong Kong, Shatin, Hong Kong

Received 12/29/06; revised 5/7/07; accepted 6/20/07.

Grant support: Canadian Institutes of Health Research and the Elia Chair in Head & Neck Cancer Research. J.D. Mocanu is a recipient of a National Cancer Institute of Canada scholarship and an alumnus of the Canadian Institutes of Health Research Excellence in Radiation Research for the 21st Century training program. Equipment support was provided by the Canadian Foundation for Innovation and the Advanced Optical Microscopy Facility of University Health Network.

The costs of publication of this article were defrayed in part by the payment of page charges. This article must therefore be hereby marked *advertisement* in accordance with 18 U.S.C. Section 1734 solely to indicate this fact.

Requests for reprints: Fei-Fei Liu, Department of Radiation Oncology, Princess Margaret Hospital/Ontario Cancer Institute, University Health Network, 610 University Avenue, Toronto, Ontario, Canada M5G 2M9. Phone: 416-946-2123; Fax: 416-946-4586; E-mail: Fei-Fei.Liu@rmp.uhn.on.ca.

doi:10.1158/1078-0432.CCR-06-3085

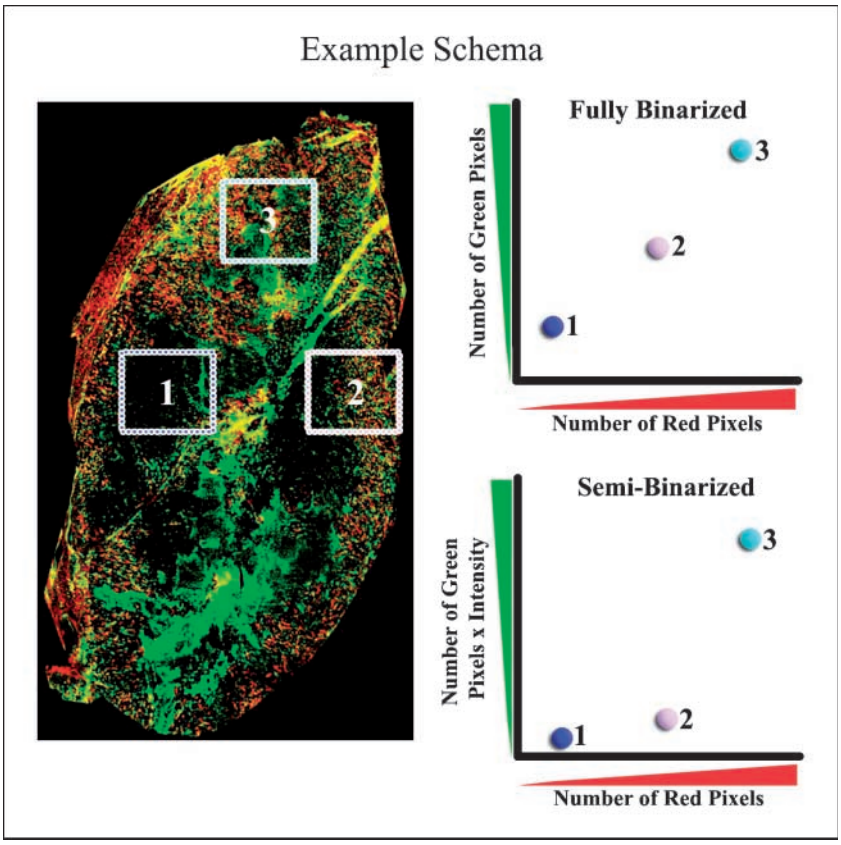

Fig. 1. A schematized representation of the generation of tumor fingerprints via large scatter plots. Sampling windows of 250 μm × 250 μm are obtained for each pixel within the tumor section. Red and green pixels within each window are then enumerated and plotted. Three examples of such windows are shown in this diagram, labeled 1 to 3, for both fully binarized (*top*) and semibinarized (*bottom*) calculations.

within human tumor models, which are potentially applicable to other therapeutic agents that can be imaged at a microscopic level (i.e., through either fluorescent or radiolabeled compound tagging).

To validate these algorithms, we introduced the antivascular agent ZD6126 to modulate the tumor microenvironment, showing a quantifiable change in the resulting ASO distribution. ZD6126 is a colchicine prodrug derivative that is metabolized *in vivo* to yield ZD6126 phenol, which then selectively binds to the colchicine-binding site of tubulin; this disrupts the microtubule structure, largely responsible for the structure and morphology of dividing and immature vascular endothelial cells (9, 13, 14). Previous studies show that this selective destabilization of the vascular endothelium results in increased leakage and occlusion, followed by the formation of large necrotic regions (9, 13), and an associated reduction in tumor IFP (9, 13).

Materials and Methods

All animal experiments were conducted with approval from the Animal Care Committee, University Health Network (Toronto, Ontario, Canada). In all cases, 6- to 8-week-old severe combined immunodeficient BALB/c mice were used. All original algorithms and programs can be found at the Liu laboratory Web page.[7]

Antisense oligonucleotides. Oligodeoxynucleotides were obtained from MoleculA and TriLink Biotech. The primary molecule used in this study was a two-base antisense mismatch control (MMC) for the Bcl-2 translation initiation site (5′-TCTCCCAGCATG*T*GCCAT-3′, mismatches italicized) labeled on the 5′ end with FITC, denoted as FITC-MMC. A molecule similar to G3139 (FITC-Bcl-2), corresponding to the first six codons of the human Bcl-2 translation initiation site (5′-TCTCCCAGCGTGCGCCAT-3′), was also used.

Cell lines and xenograft tumor models. C666-1 human nasopharyngeal carcinoma (15), CaSki cervix, and DU-145 prostate carcinoma cell lines (American Type Culture Collection) were maintained in RPMI 1640 with 10% fetal bovine serum (Wisent, Inc.) and 100 mg/L penicillin/streptomycin at 37°C, 5% CO_2. C15 nasopharyngeal carcinoma xenografts are continuously propagated *in vivo* and homogenized into single cells before use (16). C666-1, C15, and CaSki xenograft tumors were generated by injecting ~10^7 cells into the left gastrocnemius muscle; DU-145 xenografts were established s.c. (~10^7 cells). Experiments were conducted when tumors reached ~1.5 cm in diameter to maximally capture microenvironment heterogeneity. Unless otherwise stated, each experimental group consisted of three mice.

Tissue preparation. FITC-MMC (300 μg in 100 μL PBS) was injected i.v. into the mouse tail vein; 20 h later, 200 μL 2-(2-nitro-1*H*-imidazol-1-yl)-*N*-(2,2,3,3,3-pentafluoropropyl) acetamide (EF5; Ben Venue Laboratories) solution (10 mmol/L EF5, 5% dextrose, and 2.4% ethanol) was injected i.v. and i.p. for uptake and metabolism by hypoxic tissues (17). Four hours later, Hoechst 33342 (600 μg in 100 μL PBS; Sigma Chemical Co.) was injected i.v. for visualization of active vasculature (18); the mice were sacrificed 1 min later. The tumors were immediately excised, frozen in OCT compound (Bayer Corp.), and then stored at -70°C. Serial tumor sections were cut at three levels, 1,000 μm apart, with the three consecutive slides most representative of the heterogeneous tumor microenvironment selected for further study. The topmost slide was stained with Cy5-ELK3-51 antibody (1:50 dilution; a kind gift from Dr. C. Koch, University of Pennsylvania, Philadelphia, PA) that binds to EF5-protein adducts in hypoxic tissues (17). The middle slide was scanned using fluorescence microscopy to image the FITC-MMC/Hoechst 33342 and then stained

[7] http://www.uhnres.utoronto.ca/liu/ASO/

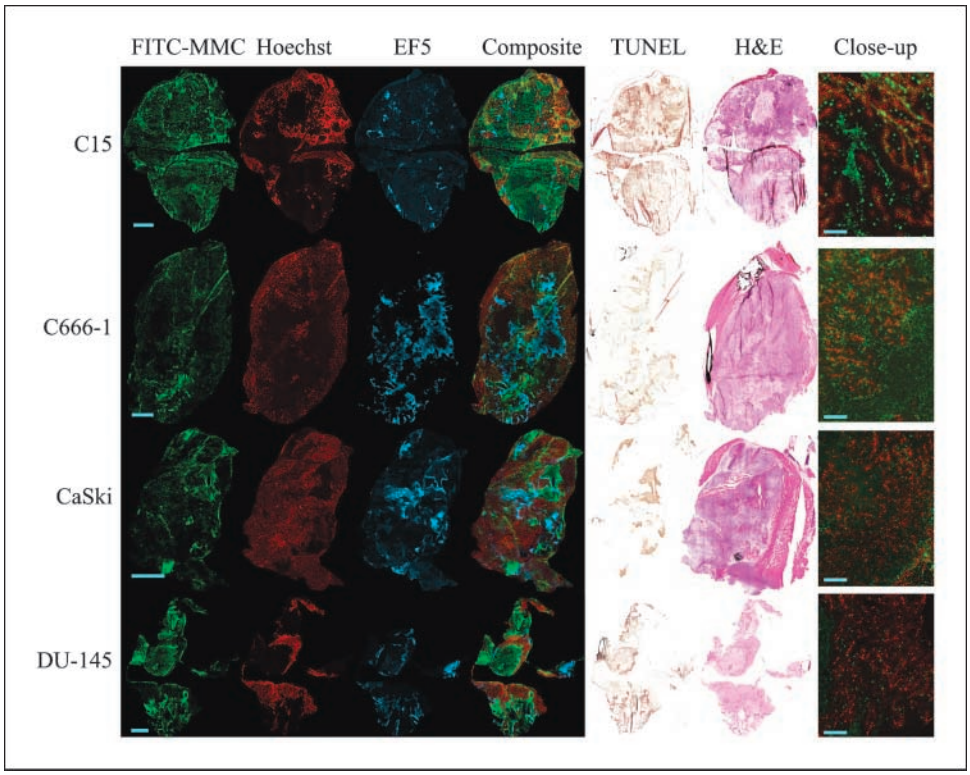

Fig. 2. Representative examples of antisense distribution (FITC-MMC) in four different xenograft tumors (C15, C666-1, CaSki, and DU-145) in relation to active vasculature (Hoechst), hypoxia (EF5), necrotic or apoptotic tissues (TUNEL), and tissue morphology (H&E). Composite images consist of FITC-MMC, Hoechst, and EF5 images superimposed, and the higher-magnification images (×50 magnification) are high-resolution representations of FITC-MMC distribution around locally active blood vessels. Bars, 2 mm (FITC-MMC images) and 250 μm ("close-up" composite images). Three mice were used per tumor type.

with terminal deoxynucleotidyl transferase–mediated dUTP nick end labeling (TUNEL) to assess apoptosis or necrosis. The bottom slide was stained with H&E. All staining and cryosectioning procedures were done by the Pathology Research Program Services, University Health Network.

Microscopy. Unstained and Cy5-anti-EF5–stained slides were imaged at ×10 magnification using an Olympus BX50 tiling fluorescence stereomicroscope (FITC: λ_{Ex} = 480 nm, λ_{Em} = 535 nm, 200 ms exposure; Hoechst 33342: λ_{Ex} = 360 nm, λ_{Em} = 460 nm, 50 ms exposure; Cy5: λ_{Ex} = 640 nm, λ_{Em} = 680 nm, 5 s exposure). Images were captured using QED*InVivo* (Media Cybernetics) and assembled using ImagePro 5.1 (Media Cybernetics). TUNEL and H&E slides were scanned using a Nikon CoolScan LS-8000 ED and an Aperio ScanScope CS automated tiling bright-field microscope.

Tumor IFP measurements. Tumor IFP was measured using a wick-in-needle apparatus consisting of a windowed needle filled with nylon suture connected to a pressure transducer with 1:10 heparin-saline–filled silicone tubing as described previously (8). Two series of measurements were obtained from three to four spatially separated locations within each tumor, either immediately before treatment with ZD6126 or vehicle or 48 h after treatment. Each experimental group consisted of six mice.

ZD6126 experiments. ZD6126 (AstraZeneca) was dissolved in 10% sodium carbonate and 90% PBS (pH 7.4, 25 mg/mL). A single 200 μL injection of either ZD6126 solution or PBS vehicle was injected i.p. into C666-1–bearing severe combined immunodeficient mice. Mice (n = 5 per group) were randomized as follows: vehicle (control, 48 h), ZD6126/0, and ZD6126/48. For the ZD6126/0 group, mice were simultaneously injected with FITC-MMC i.v. and ZD6126 i.p. The ZD6126/48 group reflects a 48-h pause following ZD6126 injection before FITC-MMC injection. Tumor IFP was measured in vehicle and ZD6126/48 groups. Animals were sacrificed and tumors were excised 6 h after FITC-MMC injection as described above. Experiments were conducted when tumors reached ~0.85 cm in diameter.

Image processing and quantitation. Fluorescence microscopy images were imported into ImageJ (NIH),[8] false colored, and merged into a composite image, where the red, green, and blue channels correspond to Hoechst 33342 (active vasculature), FITC-MMC (antisense), and Cy5-anti-EF5 (hypoxia).

For quantitation, unprocessed Hoechst 33342 and FITC-MMC images were edited in ImageJ to remove artifacts. The tumor boundary, determined by the dense regions with strong hematoxylin staining, was then traced onto each image based on corresponding H&E slides, and all nontumor pixels were erased. The images were either fully binarized or semibinarized to simplify and standardize subsequent calculations using custom software developed for this study. Briefly, an image is binarized when all pixels that exceed 1 SD of the mean pixel value are assigned a value of 1, whereas the remaining pixels are set to 0. Images containing the FITC-MMC and Hoechst 33342 channels were then processed using the following algorithm to generate tumor microenvironment scatter plots.

Each composite image was divided into overlapping windows of 100 × 100 pixels (250 × 250 μm; for sufficient detail while minimizing computation time), and within each window, the pixels indicating the presence of active vasculature (red) and/or ASO (green) were enumerated and then plotted along FITC (Y axis) and Hoechst (X axis) axes. For the experiments characterizing distribution in the different xenograft models, both FITC-MMC and Hoechst 33342 channels were binarized to minimize variability between batches of labeled antisense (schema shown in Fig. 1, *top*). For the ZD6126 experiments, only the Hoechst 33342 channel was binarized (semi-binarized analysis; Fig. 1, *bottom*), as the same batch of labeled antisense was used for all three experimental groups. Two gating variables were used to account for background levels of FITC-MMC and Hoechst signals; the FITC-MMC gate was determined from autofluorescence measurements of C666-1 tumors that do not contain ASO (intensity value of 0.0206 per pixel; data not shown). Windows containing <1% binarized Hoechst 33342 pixels were considered to be nonvascular regions. Scatter plot trend lines ($y = ax + b$)

[8] http://rsb.info.nih.gov/ij/

were calculated using the standard linear regression equation based on minimizing the sum of squared residuals where:

$$a = \frac{\sum(x_i - x_{avg})(y_i - y_{avg})}{\sum(x_i - x_{avg})^2}$$

Statistical analyses. All statistical tests were done using two-tailed, unpaired, heteroscedastic Student's *t* tests, with a confidence level $P \leq 0.05$ defining significance. Unless otherwise stated, plotted values reflect the mean ± SD.

Results

Microdistribution of FITC-MMC in four human xenograft models. We used the fluorescent FITC-MMC molecule, known to have minimal effect on tumor behavior, to examine ASO microdistribution (12, 19, 20). Two nasopharyngeal (C15 and C666-1), one cervix (CaSki), and one prostate cancer (DU-145) xenograft models were chosen to show intramodel and intermodel variation. Figure 2 shows FITC-MMC distribution in a single representative tumor (out of three examined) for each model, in relation to active vasculature (visualized by Hoechst 33342), hypoxia (EF5), necrosis or apoptosis (TUNEL), and tissue morphology (H&E). An unexpected observation was the apparent colocalization of ASO molecules to regions of necrotic/apoptotic tissue (TUNEL positive), which has not been described previously. As expected, regions of hypoxia (EF5 positive) were observed to outline the periphery of TUNEL-positive regions, suggesting that these regions were nonviable before the administration of the ASO. These observations are particularly evident in the CaSki and DU-145 xenografts that have clearly defined necrotic regions (Fig. 2, *bottom*). To address the possibility that the MMC sequence might have distributed differently than a biologically active molecule due to the absence of an oligonucleotide "target," these studies were repeated using FITC-Bcl-2 in C15 tumors, which express high levels of *bcl-2* (12); no difference in ASO biodistribution was observed (data not shown).

Each xenograft model has a unique and consistent antisense distribution "fingerprint." This scatter plot method (Fig. 3) essentially provides a fingerprint of the physical environment within each individual tumor based on ASO drug distribution and active vasculature. Each tumor type seemed to have a unique pattern, with all three separate tumors within each model sharing that same general pattern. The C666-1 plots were very distinct from the C15, CaSki, and DU-145, showing a linear increase of ASO with vasculature and a minimal ASO-rich margin from sampling windows that have sparse active vasculature. The CaSki and DU-145 patterns were nearly identical, with a strong bimodal distribution indicating no

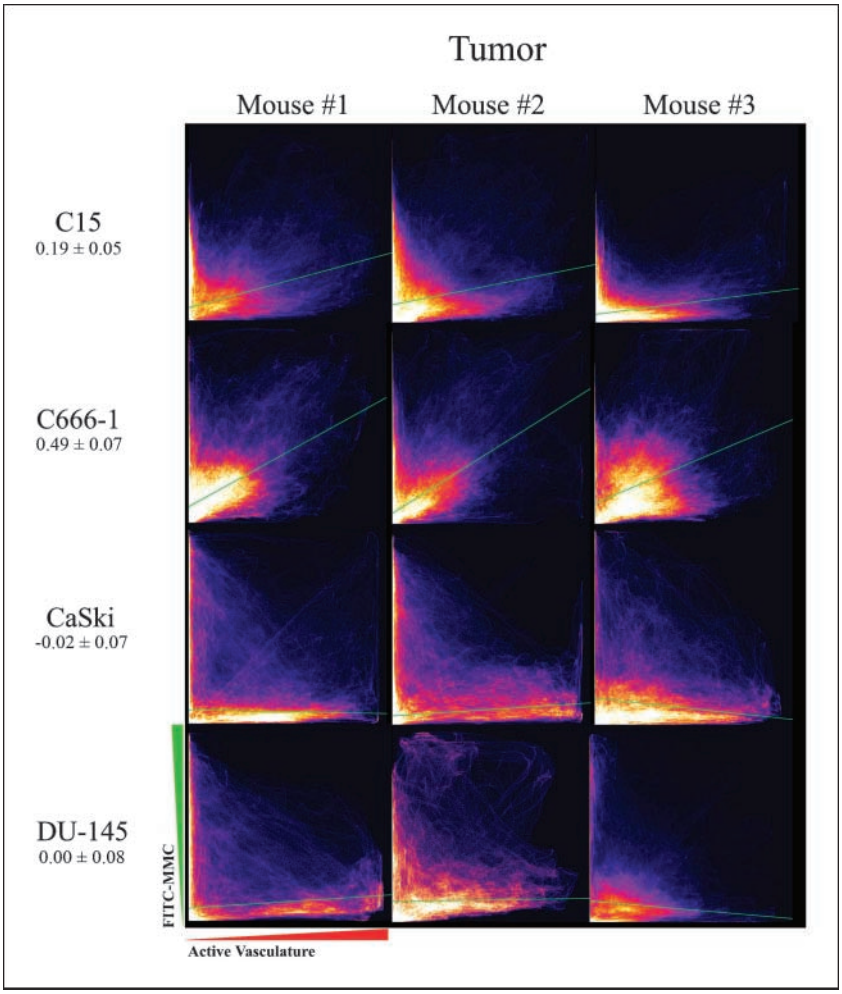

Fig. 3. Scatter plots of antisense molecules versus vasculature for each xenograft tumor. *X* axis, increasing counts of active vasculature pixels; *Y* axis, increasing counts of FITC-MMC pixels. Each data point represents one sampling window. Bright green line, slope fitting the linear region of each scatter plot. Average slope values ± SD are indicated beneath each xenograft label. Each scatter plot represents an individual tumor.

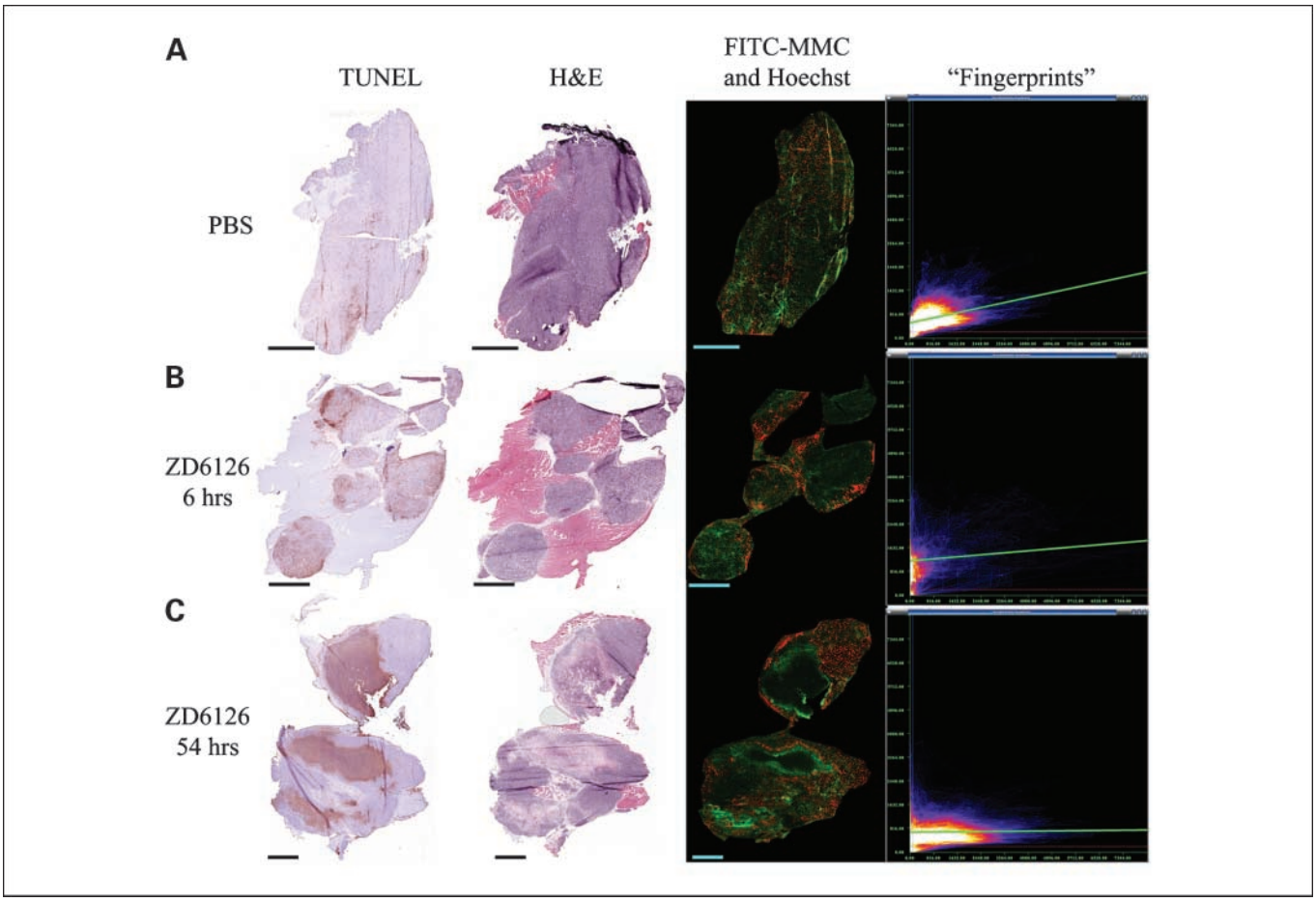

Fig. 4. The effect of ZD6126 on C666-1 tumors. Representative examples are shown of necrotic or apoptotic tissues (TUNEL), tissue morphology (H&E), and antisense with active vasculature distribution (FITC-MMC and Hoechst) in C666-1 tumors under three treatment conditions: (*A*) vehicle control (PBS), (*B*) 6 h after ZD6126 treatment and FITC-MMC injection (ZD6126, 6 h), and (*C*) 54 h after ZD6126 treatment and 6 h after FITC-MMC injection (ZD6126, 54 h). Each group consisted of five mice. Bar, 2 mm. Far right column, semibinarized fingerprints of the representative tumors, where the *X* axes represent active vascular density, whereas the *Y* axes represent the amount of FITC-MMC. Bright green line, slope; red and blue lines, used gating values for FITC background and delineation of necrotic regions as mentioned in Materials and Methods.

significant relationship between ASO distribution and active vasculature.

When the vascular regions (signified by the presence of Hoechst 33342 pixels) of these scatter plots were fitted with trend lines, the slopes indicated significant differences between each tumor model ($P < 0.03$), with the exception of CaSki versus DU-145, which was expected because their scatter plot patterns are very similar (Fig. 3). The slope values reflect the quantity of antisense present in the tumor in relation to vascular size or density, as the blood vessel sizes are not similar across all four models. A positive slope indicates a correlation between quantities of antisense with increasing active vasculature; a negative slope indicates a decrease in antisense as vasculature increases. There was no significant relationship observed with the *Y*-intercept values of the trend lines.

Time-dependent effects of ZD6126 on C666-1 vasculature and cell viability. The validity of the scatter plot approach was then shown by modulating the tumor microenvironment through the use of the potent vascular disrupting agent ZD6126. Figure 4 shows the significant vascular destructive effect associated with this drug when given 48 h before FITC-MMC injection versus simultaneous injections. C666-1 tumors treated with ZD6126 and FITC-MMC simultaneously, examined 6 h later, all showed punctate regions of apoptosis/necrosis accompanied by nearly no active vascular function within tumor tissues (Fig. 4B). In contrast, tumors isolated 54 h after ZD6126 injection (48 h after ZD6126 plus 6 h after FITC-MMC) all displayed large regions of disseminated necrosis (Fig. 4C).

The effects of ZD6126 on antisense distribution and tumor IFP in C666-1 xenografts. The slopes of linear regression trend lines fitted to the scatter plots indicate a significant difference between the ZD6126 treated versus vehicle controls (Fig. 5A). Because the vasculature of C666-1 tumors consists of microcapillaries with similar diameters (Fig. 2, *top right*), the slope values reflect the quantity of antisense in the tumor in relation to vascular density. This analysis was semibinarized as the same stock of FITC-MMC was used; hence, the values reflect not only the presence of FITC-MMC pixels within sampling windows but also their intensities as well. This ultimately increases the accuracy of the experimental approach.

Mice treated with ZD6126 showed significantly flatter slopes of 0.10 (examined at 6 h) and 0.17 (at 54 h) compared with

0.37 of the vehicle control (P = 0.003 or 0.029, respectively). These results suggest that, despite the presence of functional vascular regions in ZD6126-treated tumors, the ASO distribution was significantly poorer compared with that of control tumors. The slope values do not account for ASO localizing to large avascular regions present within the ZD6126-treated tumors.

Figure 5B illustrates a significant reduction in tumor IFP in the C666-1 tumors (P = 0.045) consequent to ZD6126 treatment (0.8 mmHg versus 13.9 mmHg for treated versus control tumors, respectively), which did not improve the relationship between ASO distributions as a function of tumor vasculature in this particular xenograft model.

Discussion

These tiled microscopy data show for the first time the relationship between antisense microdistribution and tumor vasculature, hypoxia, and apoptosis/necrosis, supplementing previous studies that evaluated whole tissue antisense biodistribution (11, 21). We have also developed an objective method to analyze the microdistribution patterns of ASO in relation to active vasculature through the use of novel quantitative algorithms. These algorithms reveal a unique yet consistent microdistribution fingerprint for each xenograft model (Fig. 3), which is significantly altered following administration of a vascular destructive agent ZD6126 (Figs. 4 and 5).

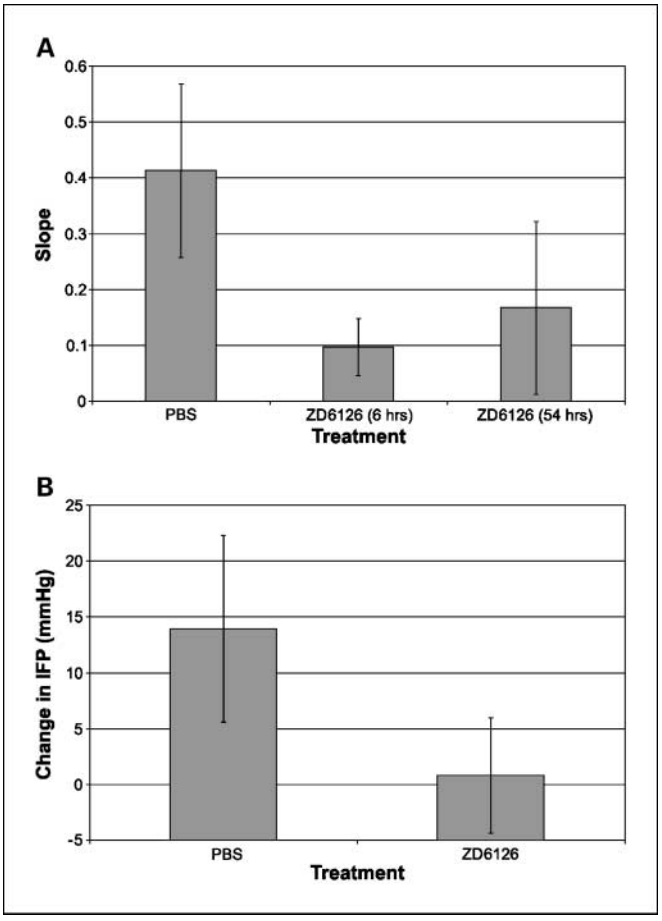

Fig. 5. Quantitative differences in IFP and slope in ZD6126 and vehicle-treated animals. *A,* slopes (n = 5 per group) from the linear regression analysis of the scatter plots or fingerprints. *B,* changes in IFP (n = 6 per group) before and 48 h after injection with either ZD6126 or vehicle (PBS).

One of the most interesting observations from this study was the unexpected colocalization of ASO molecules with regions of apoptosis or necrosis (Figs. 2 and 4), which might in part account for the resistance of solid tumors to these therapies (10, 12). This observation with ASOs is distinct from other anticancer agents, such as doxorubicin, which fail to reach hypoxic regions due to limited diffusion from active blood vessels (22, 23). The mechanism for the apparent ASO accumulation remains unknown, although possibilities could include heterogeneity of tumor IFP, diffusion from surrounding vessels, charge effects, or unknown efflux/retention mechanisms of ASO molecules.

Another interesting observation relates to the lack of tumor IFP reduction improving ASO distribution, in contrast to those reported for other drugs (24, 25). One would expect that a decrease in IFP would increase the amount of ASO leaving the microcirculation as the density of blood vessels increased, but this was not observed. This might possibly be related to the significant necrosis induced by ZD6126 and the peculiar association between ASO molecules with regions of necrosis/hypoxia. Alternatively, the surviving/new tumor vasculature might not be as permeable to ASO in comparison with vehicle-treated animals (Fig. 5A). Finally, other variables, such as the amount of collagen or the status of other fibrillar interstitial proteins that could affect ASO distribution, which were not measured for this study, may be involved.

The analytic techniques presented in this study could be applied to other therapeutic agents, such as antibodies, viruses, or small-molecule inhibitors. The correlating variables need not be restricted to vasculature, hypoxia, or apoptosis; other fluorescent markers of the therapeutic molecule could also be assessed with no modifications required to this algorithm. This methodology could also be automated for high-throughput capability where, for example, several compounds and conditions could be evaluated through the use of automated fluorescence microscopes, which are emerging technologies, such as the TISSUEscope by Biomedical Photometrics. Finally, it would be of interest to determine whether a particular biodistribution pattern could predict for therapeutic benefit of a single agent or a combination of two or more agents.

In conclusion, the use of algorithms and techniques similar to those described in this report may lead to the development of standardized drug distribution fingerprints for individual tumor models based on variables such as vasculature, hypoxia, and necrosis/apoptosis. In conjunction with molecular and biochemical data, these analyses will contribute to another dimension in achieving greater insight into the potential efficacy of molecular cancer therapeutic agents.

Acknowledgments

We thank James Jonkman, Gillian Sleep, Andy Primeau, and the Pathology Research Program Services for their technical support and valuable input.

References

1. Vaupel P, Kallinowski F, Okunieff P. Blood flow, oxygen and nutrient supply, and metabolic microenvironment of human tumors: a review. Cancer Res 1989; 49:6449–65.

2. Helmlinger G, Yuan F, Dellian M, Jain RK. Interstitial pH and pO_2 gradients in solid tumors *in vivo*: high-resolution measurements reveal a lack of correlation. Nat Med 1997;3:177–82.

3. Neri D, Bicknell R. Tumour vascular targeting. Nat Rev Cancer 2005;5:436–46.

4. Jain RK. Delivery of molecular and cellular medicine to solid tumors. Adv Drug Deliv Rev 2001;46:149–68.

5. Brown JM, Wilson WR. Exploiting tumour hypoxia in cancer treatment. Nat Rev Cancer 2004;4:437–47.

6. Thomlinson RH, Gray LH. The histological structure of some human lung cancers and the possible implications for radiotherapy. Br J Cancer 1955;9:539–49.

7. Gottesman MM, Fojo T, Bates SE. Multidrug resistance in cancer: role of ATP-dependent transporters. Nat Rev Cancer 2002;2:48–58.

8. Milosevic MF, Fyles AW, Wong R, et al. Interstitial fluid pressure in cervical carcinoma: within tumor heterogeneity, and relation to oxygen tension. Cancer 1998;82:2418–26.

9. Skliarenko JV, Lunt SJ, Gordon ML, Vitkin A, Milosevic M, Hill RP. Effects of the vascular disrupting agent ZD6126 on interstitial fluid pressure and cell survival in tumors. Cancer Res 2006;66:2074–80.

10. Gleave ME, Monia BP. Antisense therapy for cancer. Nat Rev Cancer 2005;5:468–79.

11. Crooke ST. Progress in antisense technology. Annu Rev Med 2004;55:61–95.

12. Yip KW, Mocanu JD, Au PY, et al. Combination bcl-2 antisense and radiation therapy for nasopharyngeal cancer. Clin Cancer Res 2005;11:8131–44.

13. Blakey DC, Westwood FR, Walker M, et al. Antitumor activity of the novel vascular targeting agent ZD6126 in a panel of tumor models. Clin Cancer Res 2002;8: 1974–83.

14. Micheletti G, Poli M, Borsotti P, et al. Vascular-targeting activity of ZD6126, a novel tubulin-binding agent. Cancer Res 2003;63:1534–7.

15. Cheung ST, Huang DP, Hui AB, et al. Nasopharyngeal carcinoma cell line (C666-1) consistently harbouring Epstein-Barr virus. Int J Cancer 1999;83: 121–6.

16. Busson P, Ganem G, Flores P, et al. Establishment and characterization of three transplantable EBV-containing nasopharyngeal carcinomas. Int J Cancer 1988;42:599–606.

17. Evans SM, Hahn S, Pook DR, et al. Detection of hypoxia in human squamous cell carcinoma by EF5 binding. Cancer Res 2000;60:2018–24.

18. Trotter MJ, Chaplin DJ, Durand RE, Olive PL. The use of fluorescent probes to identify regions of transient perfusion in murine tumors. Int J Radiat Oncol Biol Phys 1989;16:931–4.

19. Gleave M, Tolcher A, Miyake H, et al. Progression to androgen independence is delayed by adjuvant treatment with antisense Bcl-2 oligodeoxynucleotides after castration in the LNCaP prostate tumor model. Clin Cancer Res 1999;5:2891–8.

20. Benimetskaya L, Wittenberger T, Stein CA, et al. Changes in gene expression induced by phosphorothioate oligodeoxynucleotides (including G3139) in PC3 prostate carcinoma cells are recapitulated at least in part by treatment with interferon-β and -γ. Clin Cancer Res 2004;10:3678–88.

21. Wang J, Chen P, Mrkobrada M, Hu M, Vallis KA, Reilly RM. Antisense imaging of epidermal growth factor-induced p21WAF-1/CIP-1 gene expression in MDA-MB-468 human breast cancer xenografts. Eur J Nucl Med Mol Imaging 2003;30:1273–80.

22. Huxham LA, Kyle AH, Baker JHE, Nykilchuk LK, Minchinton AI. Microregional effects of gemcitabine in HCT-116 xenografts. Cancer Res 2004;64: 6537–41.

23. Lankelma J, Dekker H, Fernandez Luque R, et al. Doxorubicin gradients in human breast cancer. Clin Cancer Res 1999;5:1703–7.

24. Pietras K, Rubin K, Sjoblom T, et al. Inhibition of PDGF receptor signaling in tumor stroma enhances antitumor effect of chemotherapy. Cancer Res 2002; 62:5476–84.

25. Tong RT, Boucher Y, Kozin SV, Winkler F, Hicklin DJ, Jain RK. Vascular normalization by vascular endothelial growth factor receptor 2 blockade induces a pressure gradient across the vasculature and improves drug penetration in tumors. Cancer Res 2004;64: 3731–6.